nature nanotechnology

LETTERS

https://doi.org/10.1038/s41565-021-01020-0



# Two-dimensional quantum-sheet films with sub-1.2 nm channels for ultrahigh-rate electrochemical capacitance

Wenshu Chen[1,2], Jiajun Gu[1]✉, Qinglei Liu[1]✉, Mengzhao Yang[1], Cheng Zhan[3], Xining Zang[4], Tuan Anh Pham[3], Guangxiang Liu[2], Wang Zhang[1], Di Zhang[1]✉, Bruce Dunn[5] and Y. Morris Wang[5]✉

**Dense, thick, but fast-ion-conductive electrodes are critical yet challenging components of ultrafast electrochemical capacitors with high volumetric power/energy densities[1–4]. Here we report an exfoliation–fragmentation–restacking strategy towards thickness-adjustable (1.5–24.0 µm) dense electrode films of restacked two-dimensional 1T-$MoS_2$ quantum sheets. These films bear the unique architecture of an exceptionally high density of narrow (sub-1.2 nm) and ultrashort (~6.1 nm) hydrophobic nanochannels for confinement ion transport. Among them, 14-µm-thick films tested at 2,000 mV $s^{-1}$ can deliver not only a high areal capacitance of 0.63 F $cm^{-2}$ but also a volumetric capacitance of 437 F $cm^{-3}$ that is one order of magnitude higher than that of other electrodes. Density functional theory and ab initio molecular dynamics simulations suggest that both hydration and nanoscale channels play crucial roles in enabling ultrafast ion transport and enhanced charge storage. This work provides a versatile strategy for generating rapid ion transport channels in thick but dense films for energy storage and filtration applications.**

High volumetric power/energy densities are indispensable when supercapacitors need to meet urgent demands in rapid-response and limited-space applications, such as regenerative braking, grid power buffers and burst-mode power delivery systems[1–4]. To realize such requirements, it is crucial to achieve electrodes that can deliver high volumetric capacitances ($C_v$) under ultrahigh rates[5–8]. Additionally, the electrodes should also deliver industrially acceptable areal capacitances ($C_a$) for practical applications (for example, 0.6 F $cm^{-2}$ for currently commercialized activated-carbon electrodes at low rates)[1,4,9]. An electrode with a higher $C_a$ allows for fewer passive components (for example, current collectors, separators and connectors) to achieve a definite total capacitance. This is critical for translating the electrode performance to a practical device[1,4,10,11].

Unfortunately, electrodes operating under ultrahigh rates (≥1,000 mV $s^{-1}$) face tough challenges in simultaneously achieving high $C_a$ and high $C_v$ (refs. [12–15]). It is difficult to enhance both mass loadings and packing densities of active materials in electrodes without obviously sacrificing ion transport dynamics[5,16–19]. To date, high $C_v$ values at 1,000 mV $s^{-1}$ have been attained in some ultrathin dense electrodes of restacked large sheets (LSs, hundreds of nanometres in their lateral sizes) of two-dimensional (2D) materials, for example, 330 F $cm^{-3}$ for 330-nm-thick 2D $TaS_2$ LS films[20], 160 F $cm^{-3}$ for 1-µm-thick 2D 1T-$MoS_2$ LS films[21] and 800 F $cm^{-3}$ for 3-µm-thick 2D $Ti_3C_2T_x$ LS films[17]. This is attributed to their sufficient interplanar active sites and vertically short ion diffusion distances; however, low mass loadings (0.16–1.17 mg $cm^{-2}$) of active materials therein cause low $C_a$ values (~0.01–0.24 F $cm^{-2}$). In contrast, well-tailored large channels for ion transport help achieve high $C_a$ values at 1,000 mV $s^{-1}$ in thick electrodes with high mass loadings of active materials (for example, 0.54 F $cm^{-2}$ for 180-µm-thick macroporous $Ti_3C_2T_x$ films[17] and 0.64 F $cm^{-2}$ for 320-µm-thick films of vertically aligned $Ti_3C_2T_x$ LSs[18]); however, their loose structures (relative densities <6.0%) inevitably lead to low $C_v$ values (~20–30 F $cm^{-3}$).

The above dilemma is related to channel utilization for ion transport, especially under high rates. For 2D material sheets, the vertical stacking mode facilitates ion transport under electrical driving force[22,23]. This strategy could yield thickness-independent capacitance in $Ti_3C_2T_x$ electrodes[18], but at the expense of $C_v$ due to macropores. In contrast, the horizontal stacking mode is more efficient at building dense electrodes with atomically defined channels with widths approaching the diameters of hydrated ions[14,16]. This could enable fast ion transport via various enhancement mechanisms (for example, Grotthuss confinement transport for protons[24] and configuration adjustment transport for hydrated alkali ions[25]). However, such transport abilities drastically decrease with the increased transport distance[26,27]. Thus, obtaining a large volume of fully interconnected ultrashort (for example sub-10 nm, ref. [26]) nanochannels is attractive when looking to achieve dense electrodes with extraordinary energy/power attributes[28], but remains a challenge to date.

Here we generate 2D 1T-$MoS_2$ quantum-sheet (QS) electrodes with mass densities comparable to their bulk materials but with ultrafast ion transport ability. These electrodes not only provide a tenfold increase in vertical ion transport nanochannels per unit area but also tenfold shorter horizontal interplanar-ion-diffusion lengths than their 2D LS counterparts (Fig. 1a). After hydration, these narrow (<1.2 nm) but short channels (~6.1 nm) exhibit a weaker degree of ionophilicity, for example, to hydronium ($H_3O^+$), which facilitates fast ion transport through a confinement transport mechanism. Thus, the optimal electrode architecture of fully interconnected ion-fast-transport structural units enables these dense electrodes to deliver an outstanding energy storage performance in various electrolytes.

[1]State Key Laboratory of Metal Matrix Composites, Shanghai Jiao Tong University, Shanghai, China. [2]School of Environmental Science and Nanjing Key Laboratory of Advanced Functional Materials, Nanjing Xiaozhuang University, Nanjing, China. [3]Physical and Life Sciences Directorate, Lawrence Livermore National Laboratory, Livermore, CA, USA. [4]Department of Materials Science and Engineering, Massachusetts Institute of Technology, Cambridge, MA, USA. [5]Department of Materials Science and Engineering, University of California, Los Angeles, Los Angeles, CA, USA. ✉e-mail: gujiajun@sjtu.edu.cn; liuqinglei@sjtu.edu.cn; zhangdi@sjtu.edu.cn; ymwang@ucla.edu

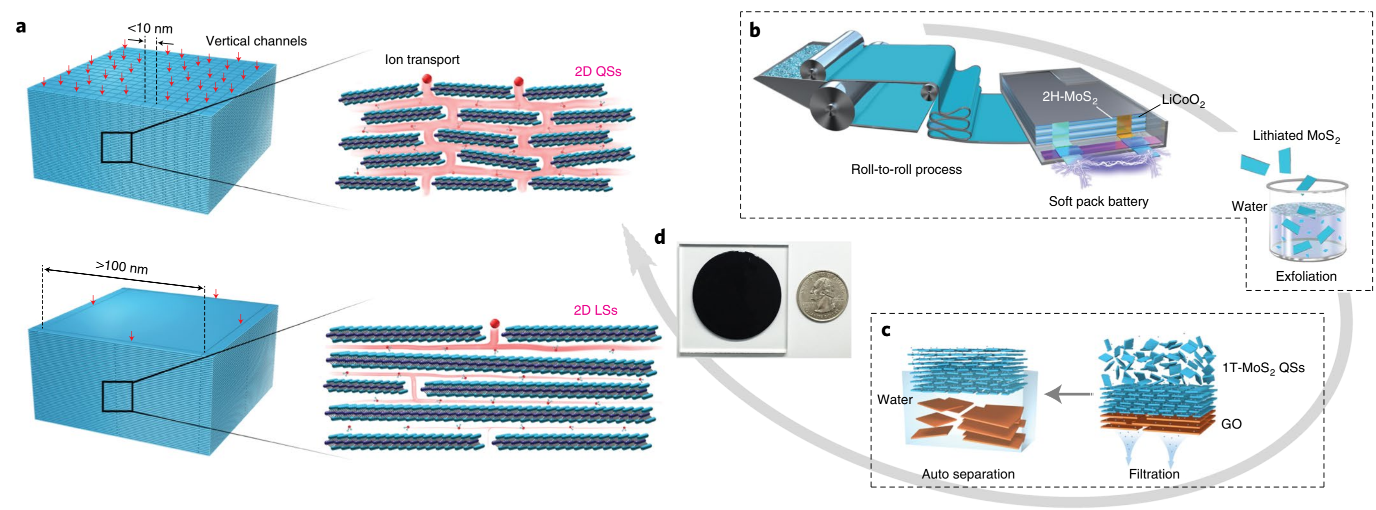


**Fig. 1 | Schematic of the design and fabrication of 2D 1T-$MoS_2$ QS films. a**, Comparison of electrolyte-ion transport in a 2D QS film and a 2D LS film under ultrahigh rates. **b**, Gram-scale 1T-$MoS_2$ QSs fabricated by controlled charging of a 2H-$MoS_2$//$LiCoO_2$ soft pack battery and exfoliating the lithiated $MoS_2$ anode in water. **c**, 1T-$MoS_2$ QS films formed via GO-assisted vacuum filtration and autoseparation from the support in water. **d**, An intact 1T-$MoS_2$ QS film (38 mm in diameter).

To realize this architecture, gram-scale single-layered 1T-$MoS_2$ QSs were first prepared via a quasi-full electrochemical Li intercalation plus water exfoliation approach on micrometre-sized 2H-$MoS_2$ particles. Here, we developed a full battery configuration (2H-$MoS_2$//$LiCoO_2$) in which 2H-$MoS_2$ anodes and $LiCoO_2$ cathodes (Supplementary Fig. 1) were premanufactured with an industry comparable roll-to-roll process (Fig. 1b and Supplementary Figs. 2 and 3). We slowly charged ($10^{-3}$ A $g^{-1}$) the soft pack batteries to 3.2 V (Supplementary Fig. 4) to realize a quasi-full transition of the $MoS_2$ materials from semiconducting 2H phase to electrically conductive 1T phase[29]. Next, we place the lithiated anodes in water and ultrasonicated them to fully shatter the $MoS_2$ particles into 2D QSs[29,30]. By centrifuging the resulting suspensions, we obtained ~1.2 g of 1T-$MoS_2$ QSs (6.1 ± 1.1 nm in lateral size and ~93 wt% in 1T phase purity) from one soft pack battery (~27 wt% yield; Supplementary Figs. 5–8).

Restacking 2D nanosheets with sizes below 10 nm to form pure QS films is challenging, as traditional filtration membranes that are widely used for restacking 2D LS films have larger pore sizes than these ultrafine QS materials. To address this challenge, we developed a graphene oxide (GO)-assisted vacuum filtration process to fabricate binder-free 1T-$MoS_2$ QS films (Fig. 1c and Supplementary Fig. 9). Typically, a thin GO film (dozens of nanometres in thickness) was preformed by filtrating a water suspension of GO LSs on a cellulose acetate membrane. After that, 1T-$MoS_2$ QSs were gradually restacked on the GO film to form a dense layer (91–98% relative densities to bulk 1T-$MoS_2$, depending on the mass loadings and the hydration status) by a second vacuum filtration treatment. The resulting 1T-$MoS_2$/GO/cellulose sandwich film was immersed in water to collapse the GO layer and separate the 1T-$MoS_2$ layer from the support (Supplementary Figs. 10 and 11a). The resulting 1T-$MoS_2$ QS film is negatively charged and can be easily transferred onto a substrate (Figs. 1d and 2a–c and Supplementary Fig. 11b). The GO filtration membranes are crucial to the formation of 2D QS films: (1) they offer smooth surfaces to the deposition of QSs and interconnected interlayer channels for water filtration, allowing the gradually quasi-parallel arrangement of QSs on their surfaces; (2) they can be autoseparated in water, avoiding the usage of acetone as in the case of cellulose acetate membranes and ensuring water is confined in the resulting QS films. The confined water greatly reduces the contact angles of various liquids from 78–82° on dehydrated films to 24–38° here (Supplementary Fig. 12) and plays an important role in achieving fast ion transport.

The dehydrated 1T-$MoS_2$ QS films with different thicknesses (1.5–24.0 μm) exhibit a typical layered structure similar to other 2D-material-based LS films[17,21,31] obtained via vacuum filtration (Fig. 2d–i). Quasi-parallel 1T-$MoS_2$ QSs alternately stack approximately along the $[001]_{1T\text{-}MoS2}$ direction via van der Waals forces between the neighbouring QSs (Supplementary Fig. 13). This vertical stacking behaviour is also supported by X-ray diffractometry (XRD) results that exhibit only $(00l)_{1T\text{-}MoS2}$ diffractions (Fig. 2b). However, unlike 2D LSs above 100 nm in lateral size[17,21,31], several 1T-$MoS_2$ QSs prefer to pack up along the $[001]_{1T\text{-}MoS2}$ direction and form a QS domain with a typical size of 4–6 nm (Fig. 2b, j, k). Zig-zag nanochannels exist between these domains (Fig. 2k and Supplementary Fig. 14a–c), and these might originate from water flowing during the filtration. A statistical analysis based on transmission electron microscopy (TEM) observations quantitively reveals the inclined horizontal arrangement of QSs (Fig. 2l and Supplementary Fig. 14). The electrical conductivity of the 1T-$MoS_2$ QS films is ~2–10 S $cm^{-1}$ (measured using a four-probe method under ambient conditions), which is about one order of magnitude lower than that of the 1T-$MoS_2$ LS films[21] because of the increased interface resistance. Grazing-incidence wide-angle X-ray scattering analyses indicate that the stacking mode of QSs in hydrated samples is similar to that in the dehydrated films (Supplementary Fig. 15). The average (001) spacing of the restacked 1T-$MoS_2$ QSs varies from 0.62 ± 0.04 nm for dehydrated films to 1.17 ± 0.15 nm for fully hydrated films (Fig. 2b) based on XRD measurements. The capillary widths for the dehydrated and hydrated films are estimated to be less than 0.685 and 1.235 nm (that is, sub-1.2 nm), respectively, based on TEM observations (Supplementary Fig. 16), which shows a channel width distribution of 0.3–1.3 nm for the dehydrated films with a peak width around 0.62 nm.

We evaluated the electrochemical performance of hydrated 1T-$MoS_2$ QS films as supercapacitor electrodes in a 0.5 M $H_2SO_4$ electrolyte (Fig. 3 and Supplementary Fig. 17). The cyclic voltammograms of a 1.5-μm-thick QS electrode exhibits a typical electric double-layer capacitor (EDLC) behaviour with scan rates up to 10,000 mV $s^{-1}$ (Fig. 3a). This delivers a capacitance of 254 F $g^{-1}$ or 1,248 F $cm^{-3}$ at 5 mV $s^{-1}$ (Fig. 3b and Supplementary Fig. 17h), which is nearly twice that of a 1-μm-thick electrode of 2D 1T-$MoS_2$

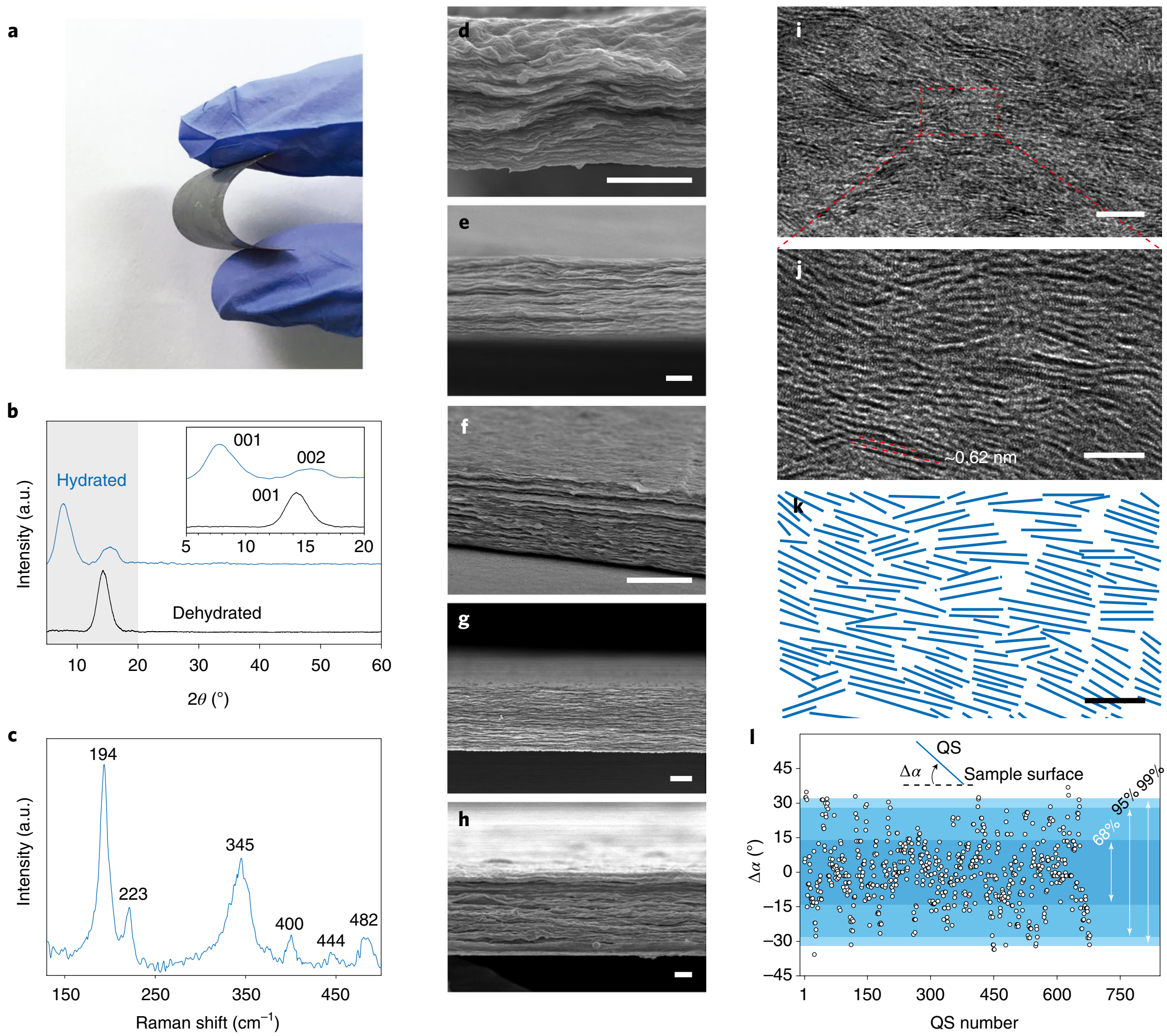


**Fig. 2 | Characterizations of 2D 1T-$MoS_2$ QS films. a**, A hydrated QS film transferred onto a flexible Au/polyimide substrate. **b**, XRD results of the hydrated and dehydrated films. **c**, Raman spectrum of the dehydrated film. **d–h**, Side-view SEM images of dehydrated films with different thicknesses 1.5 µm (**d**), 3.0 µm (**e**), 6.0 µm (**f**), 14.0 µm (**g**) and 24.0 µm (**h**). **i**, Cross-sectional TEM observations. **j**, Close-up view of **i**. **k**, Stacking mode of the 2D QSs extracted from **j**. **l**, Statistical analysis of the deviation angle ($\Delta\alpha$) distribution for 678 individual QSs based on TEM observations, where 1$\sigma$ (68%) is (–14°, 14°), 2$\sigma$ (95%) is (–28°, 28°) and 3$\sigma$ (99%) is (–32°, 32°). Scale bars: **d**,**e**, 1 µm; **f**–**h**, 5 µm; **i**, 20 nm; **j**,**k**, 5 nm. a.u., arbitrary units.

LSs[21]. The capacitance slightly decreases with increased scan rates, but remains at 143 F $g^{-1}$ and 703 F $cm^{-3}$ even under 2,000 mV $s^{-1}$. A similar rate-dependent fading tendency in $C_v$ was also observed on thicker (up to 24.0 µm) QS electrodes (Fig. 3b and Supplementary Fig. 17g). In comparison, the reported $C_v$ for 1-µm-thick 1T-$MoS_2$[21] and 3-µm-thick $Ti_3C_2T_x$ (ref. [17]) LS-based dense electrodes faded rapidly when the scan rates were over 200 mV $s^{-1}$. The $C_v$ of 13- and 40-µm-thick $Ti_3C_2T_x$ dense electrodes[17] exhibited this tendency at scan rates even down to 20 mV $s^{-1}$. These results demonstrate the excellent rate performance of our dense 1T-$MoS_2$ QS electrodes.

Electrochemical impedance spectroscopy (EIS) results offer insight into the electron transfer and ion transport properties of the hydrated 1T-$MoS_2$ QS electrodes. The 1.5-µm-thick electrode exhibits a low charge transfer resistance ($R_{ct}$) of 0.23 Ω $cm^2$ and neglectable ion transport resistance (without a 45° Warburg-type impedance element) at all studied potentials (Supplementary Fig. 18). For thicker QS electrodes, the $R_{ct}$ increases (Supplementary Table 1; for example, 0.92 Ω $cm^2$ for a 24-µm-thick sample, Fig. 3c) due to the presence of more QS interfaces per unit area. However, the ion transport resistance of these electrodes is still less than 0.16 Ω $cm^2$, illustrating the excellent ion transport dynamics. Our comprehensive studies indicate that these 1T-$MoS_2$ QS films also exhibit high capacities in neutral electrolytes via the water-facilitated intercalation and transport of $Li^+$, $Na^+$ and $K^+$ ions between their short interplanar gaps (Supplementary Figs. 19–21), for example, 1,197 and 1,237 F $cm^{-3}$ at 5 mV $s^{-1}$ for the 1.5-µm-thick electrode in 0.5 M $Na_2SO_4$ and 1 M KCl, respectively (Supplementary Fig. 19g).

A kinetic parameter $b$ determined from the power-law relationship helps to understand the charge storage kinetics of electrodes[32,33]. Here, the $b$ value for the 1.5-µm-thick QS electrode is calculated to be 0.93. This is quite close to 1.0 and demonstrates a surface-controlled capacitive process for the hydrated QS electrodes (Fig. 3d). This behaviour is well retained for the 14- and 24-µm-thick QS electrodes until ultrahigh scan rates of 3,000 and 1,000 mV $s^{-1}$, respectively. Ex situ X-ray photoelectron spectroscopy (XPS) analysis further suggests an EDLC energy storage mechanism for these electrodes (Supplementary Fig. 22). Ex situ Raman investigation indicates that the modes of 1T-$MoS_2$ do not significantly change during cycling (Supplementary Fig. 23).

In 0.5 M $H_2SO_4$, the 1.5-µm-thick 1T-$MoS_2$ QS electrode delivers $C_a$ values of less than 0.2 F $cm^{-2}$ over the entire scan rates because of its low 1T-$MoS_2$ loading (0.75 mg $cm^{-2}$, Supplementary Fig. 17b);

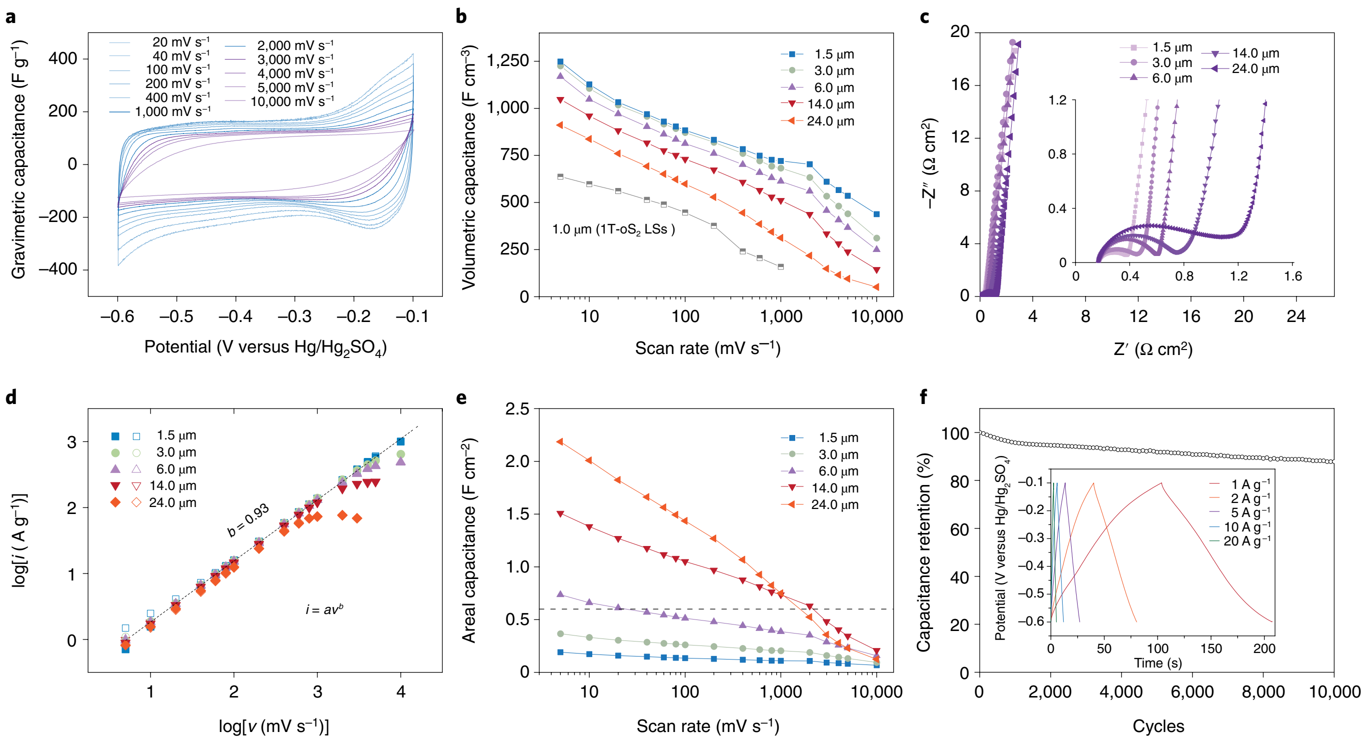


**Fig. 3 | Electrochemical performance of the hydrated 2D 1T-$MoS_2$ QS electrodes in 0.5 M $H_2SO_4$ electrolyte. a**, Cyclic voltammograms of a 1.5-µm-thick electrode over scan rates from 20 to 10,000 mV $s^{-1}$. **b**, Volumetric rate performance for 1.5- to 24-µm-thick electrodes compared with that of a 1-µm-thick 2D 1T-$MoS_2$ LS film[21]. **c**, EIS data collected at –0.3 V versus $Hg/Hg_2SO_4$ for the 1.5- to 24-µm-thick electrodes. **d**, Plot of the logarithm of anodic (filled symbols) and cathodic (open symbols) currents ($i$) versus the logarithm of scan rates ($v$) for the 1.5- to 24-µm-thick electrodes. The $b$ value is determined from the slope of the plots. Values of the current are chosen at a fixed potential of −0.3 V versus $Hg/Hg_2SO_4$. **e**, Rate dependence of areal capacitance for electrodes with different thicknesses. The dashed line shows an industrially acceptable value of 0.6 F $cm^{-2}$. **f**, Capacitance retention for a 14-µm-thick electrode under a galvanostatic cycling rate of 10 A $g^{-1}$. The inset shows the galvanostatic cycling data collected from 1 to 20 A $g^{-1}$.

however, the $C_a$ values at 1,000 mV $s^{-1}$ reach 0.74 and 0.75 F $cm^{-2}$ for 14- and 24-µm-thick 1T-$MoS_2$ QS electrodes (6.64 and 10.87 mg $cm^{-2}$ in 1T-$MoS_2$ loadings), respectively. At 2,000 mV $s^{-1}$, the 14-µm-thick electrode still delivers a $C_a$ of 0.63 F $cm^{-2}$ along with a high $C_v$ up to 437 F $cm^{-3}$, meeting the need for practical applications (Fig. 3e). In 1 M KCl, the 24-µm-thick electrode achieves a $C_a$ of 0.61 F $cm^{-2}$ and a $C_v$ of 255 F $cm^{-3}$ at 1,000 mV $s^{-1}$ (Supplementary Figs. 20f, g). Its capacitance retention is 88% at 10 A $g^{-1}$ after 10,000 cycles (Fig. 3f).

We summarized the performance of the state-of-the-art electrodes working under ultrahigh scan rates of 1,000 and 2,000 mV $s^{-1}$ (Fig. 4). The horizontal broken line indicates an industrially acceptable $C_a$ of 0.6 F $cm^{-2}$ attained by commercialized activated-carbon electrodes (scan rates ≤200 mV $s^{-1}$). This chart illustrates some breakthroughs (including our work here) in pursuing ultrahigh-rate electrodes with both high $C_a$ and $C_v$ towards miniaturized devices. For different electrodes with the same $C_a$ value, from $C_a = C_v d$, where $d$ is the electrode thickness, the thinner electrodes will have higher $C_v$ values that are preferred for supercapacitors to achieve high volumetric energy densities. To date, only vertically aligned $Ti_3C_2T_x$ LSs[18] have approached a $C_a$ about 0.6 F $cm^{-2}$ at 1,000 mV $s^{-1}$. However, the 200-µm-thick film has a $C_v$ value of ~30 F $cm^{-3}$. On the other hand, if a 1-µm-thick film is to achieve a $C_a$ of 0.6 F $cm^{-2}$ under ultrahigh scan rates, its $C_v$ must reach 6,000 F $cm^{-3}$, which is far beyond the present record. Hence, there is a suitable thickness range (~5–50 µm) for an electrode to acquire an acceptable $C_a$ of 0.6 F $cm^{-2}$ and an accessible high $C_v$ (~1200–120 F $cm^{-3}$). These require the electrode to have a unique architecture of dense active materials but abundant and highly connected fast-ion-transport channels. Historically, the 40-µm-thick restacked pseudocapacitive $Ti_3C_2T_x$ hydrogel films[17] have achieved a $C_a$ of 0.46 F $cm^{-2}$ and a $C_v$ of 115 F $cm^{-3}$ at 1,000 mV $s^{-1}$. Now, our EDLC-type 1T-$MoS_2$ QS electrodes illustrate improved performance through an optimized electrode architecture, which enhances the utilization of horizontal nanochannels (Supplementary Fig. 24). This favours ultrafast supercapacitors with high volumetric and areal energy densities.

Our density functional theory (DFT) and ab initio molecular dynamics (AIMD) simulations (Supplementary Figs. 25–32) and literature data[26,27,34] suggest that both hydration and confinement effects play crucial roles in achieving high capacitive performance in our electrodes. More specifically, DFT calculations using an implicit solvation model show that the presence of solvation can greatly weaken the proton interaction with the $MoS_2$ surface that in turn benefits ion diffusion. We found that proton binds strongly with surface sulphur atoms in vacuum while it prefers to form a hydronium ion with water in the presence of the solvation (Supplementary Fig. 26). This result is further supported by direct AIMD simulations, showing that protons always reside in the water layer confined within the hydrated $MoS_2$ channel, and diffuse via the Grotthuss mechanism (Supplementary Fig. 27 and Supplementary Video 1). Similar conclusions were obtained for alkali metal cations, where we show that solvation effects significantly weaken the ion–$MoS_2$ interaction (Supplementary Figs. 28–30, Supplementary Table 2 and Supplementary Video 2), pointing to the importance of hydration effects in facilitating ion transport. In addition, we found that confinement enhances the interfacial charge transfer between the electrolyte and electrode (Supplementary Fig. 31 and Supplementary Table 3), which has been shown to be an important

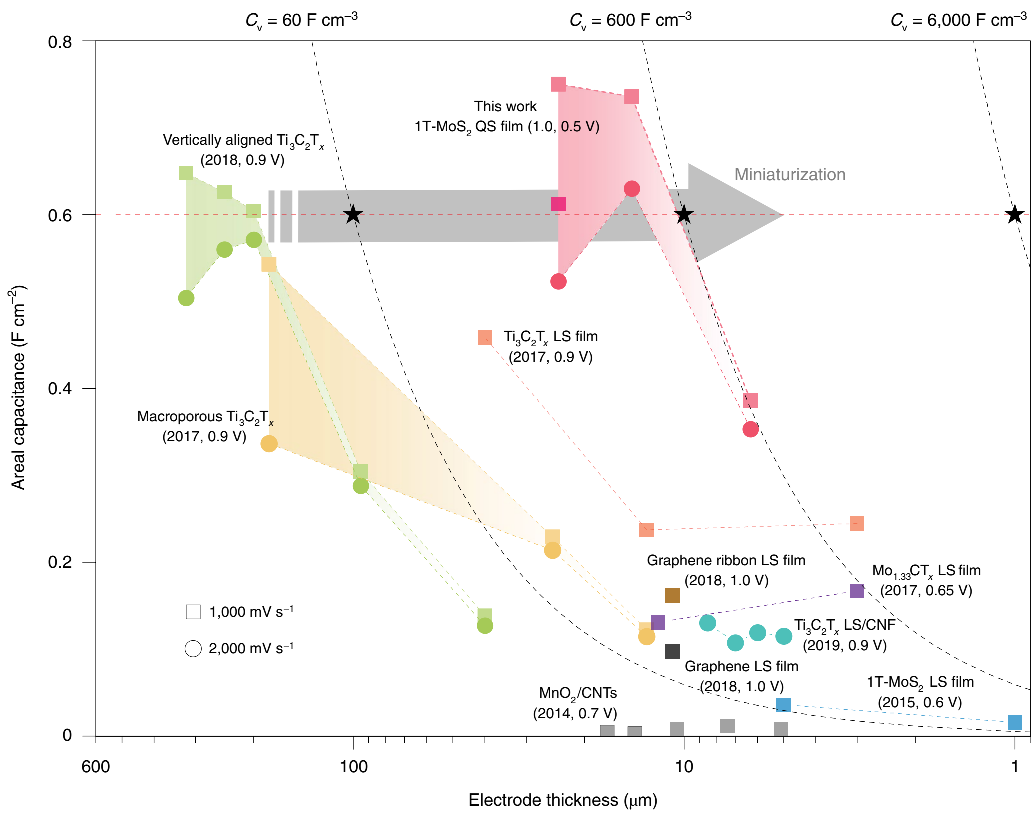


**Fig. 4 | Comparison of the $C_v$ and $C_a$ of 1T-MoS$_2$ QS electrodes with the benchmark electrodes at scan rates of 1,000 and 2,000 mV s$^{-1}$ in aqueous electrolytes.** These electrode materials include vertically aligned Ti$_3$C$_2$T$_x$ (ref. [18]), macroporous Ti$_3$C$_2$T$_x$ (ref. [17]), Ti$_3$C$_2$T$_x$ LSs[17], Mo$_{1.33}$CT$_x$ LSs[39], graphene ribbon LSs[40], graphene LSs[40], 1T-MoS$_2$ LSs[21], Ti$_3$C$_2$T$_x$ LS/cellulose nanofibre (CNF)[41] and MnO$_2$/carbon nanotubes (CNTs)[42], with testing potential window included. The data for our 1T-MoS$_2$ electrodes are based on electrochemical results in H$_2$SO$_4$ and KCl electrolytes. Three black dashed contours of $C_v$ equal to 60, 600 and 6,000 F cm$^{-3}$ were plotted, which should be attained by electrodes with 100, 10 and 1 μm thickness, respectively, to reach a $C_a$ of 0.6 F cm$^{-2}$ (shown by the three black stars).

factor in improving capacitive performance for porous materials[35]. This is in line with the observation that the calculated charge transfer increases with the ionic radius, a trend that is consistent with the measured capacitance (Supplementary Fig. 19f). We note that our conclusions on the hydration and confinement effects are not affected by whether 1T or 1T′ phases of MoS$_2$ were used in the calculations, despite the fact that the 1T′ is thermodynamically more stable (Supplementary Figs. 28 and 32 and Supplementary Tables 2–4).

Studies of proton transport in hydrophobic, ultrashort (<10 nm) nanochannels[26] indicate an order of magnitude higher diffusion constant than the bulk value when the channel width $D$ approaches 1.0 nm, due to a unique Grotthuss 'hop-turn' confinement transport mechanism[36]. When 1.0 nm < $D$ < 1.5 nm (ref. [25]), a significant enhancement of proton transport is still observed. For long nanochannels, controlled studies of various cation transport mechanisms have suggested an increased ion resistance with channel length[27], and thus a likely degradation of electrode performance in such channels. These results are in line with our observations and accentuate the importance of using ultrashort and nanometre-wide channels to achieve ultrahigh transport rates in our electrodes.

We have demonstrated that the dense 2D QS films are high-performance supercapacitor electrodes under ultrahigh rates in various aqueous-based electrolytes. Their good performance is due to the unique electrode architecture of interconnected networks of narrow but short hydrated channels, achieved by the restacking of exfoliated QSs. As the restacking approach could generate a wide range of interlayer spacing by controlling the hydration degree and no longer has the size limitations of numerous host materials, the platform offers a versatile tool to investigate the transport and storage mechanisms of a variety of ion species including single- and multi-valent ions[37,38]. We expect that our strategy is applicable to other metallic or semiconducting 2D materials, that is, lightweight materials that could achieve higher gravimetric capacitance. Further structural optimization (such as the size and shape of QSs and the degree of hydration) may help to improve the performance of 2D QS films for energy storage or filtration applications.

## Online content

Any methods, additional references, Nature Research reporting summaries, source data, extended data, supplementary information, acknowledgements, peer review information; details of author contributions and competing interests; and statements of data and code availability are available at https://doi.org/10.1038/s41565-021-01020-0.

Received: 9 February 2021; Accepted: 29 September 2021;
Published online: 18 November 2021

## References

1. Gogotsi, Y. & Simon, P. True performance metrics in electrochemical energy storage. *Science* **334**, 917–918 (2011).
2. Zhu, Y. et al. Carbon-based supercapacitors produced by activation of graphene. *Science* **332**, 1537–1541 (2011).
3. Lin, T. et al. Nitrogen-doped mesoporous carbon of extraordinary capacitance for electrochemical energy storage. *Science* **350**, 1508–1513 (2015).

4. Simon, P. & Gogotsi, Y. Perspectives for electrochemical capacitors and related devices. *Nat. Mater.* **19**, 1151–1163 (2020).
5. Augustyn, V. & Gogotsi, Y. 2D materials with nanoconfined fluids for electrochemical energy storage. *Joule* **1**, 443–452 (2017).
6. Choi, C. et al. Achieving high energy density and high power density with pseudocapacitive materials. *Nat. Rev. Mater.* **5**, 5–19 (2019).
7. Gao, T. et al. 3D printing of tunable energy storage devices with both high areal and volumetric energy densities. *Adv. Energy Mater.* **9**, 1802578 (2019).
8. Jiang, K. et al. Interfacial approach toward benzene-bridged polypyrrole film–based micro-supercapacitors with ultrahigh volumetric power density. *Adv. Funct. Mater.* **30**, 1908243 (2020).
9. Feng, D. et al. Robust and conductive two-dimensional metal−organic frameworks with exceptionally high volumetric and areal capacitance. *Nat. Energy* **3**, 30–36 (2018).
10. Sun, H. et al. Three-dimensional holey-graphene/niobia composite architectures for ultrahigh-rate energy storage. *Science* **356**, 599–604 (2017).
11. Sheberla, D. et al. Conductive MOF electrodes for stable supercapacitors with high areal capacitance. *Nat. Mater.* **16**, 220–224 (2017).
12. Koltonow, A. R. & Huang, J. Two-dimensional nanofluidics. *Science* **351**, 1395–1396 (2016).
13. Sun, H. et al. Hierarchical 3D electrodes for electrochemical energy storage. *Nat. Rev. Mater.* **4**, 45–60 (2019).
14. Li, Z. et al. Tuning the interlayer spacing of graphene laminate films for efficient pore utilization towards compact capacitive energy storage. *Nat. Energy* **5**, 160–168 (2020).
15. Li, Y. et al. A general Lewis acidic etching route for preparing MXenes with enhanced electrochemical performance in non-aqueous electrolyte. *Nat. Mater.* **19**, 894–899 (2020).
16. Yang, X., Cheng, C., Wang, Y., Qiu, L. & Li, D. Liquid-mediated dense integration of graphene materials for compact capacitive energy storage. *Science* **341**, 534–537 (2013).
17. Lukatskaya, M. R. et al. Ultra-high-rate pseudocapacitive energy storage in two-dimensional transition metal carbides. *Nat. Energy* **2**, 17105 (2017).
18. Xia, Y. et al. Thickness-independent capacitance of vertically aligned liquid-crystalline MXenes. *Nature* **557**, 409–412 (2018).
19. Pomerantseva, E., Bonaccorso, F., Feng, X. L., Cui, Y. & Gogotsi, Y. Energy storage: the future enabled by nanomaterials. *Science* **366**, eaan8285 (2019).
20. Wu, J. et al. Acid-assisted exfoliation toward metallic sub-nanopore $TaS_2$ monolayer with high volumetric capacitance. *J. Am. Chem. Soc.* **140**, 493–498 (2018).
21. Acerce, M., Voiry, D. & Chhowalla, M. Metallic 1T phase $MoS_2$ nanosheets as supercapacitor electrode materials. *Nat. Nanotechnol.* **10**, 313–318 (2015).
22. Yoo, J. et al. Ultrathin planar graphene supercapacitors. *Nano Lett.* **11**, 1423–1427 (2011).
23. Yoon, Y. et al. Vertical alignments of graphene sheets spatially and densely piled for fast ion diffusion in compact supercapacitors. *ACS Nano* **8**, 4580–4590 (2014).
24. de Grotthuss, C. J. T. Sur la décomposition de l'eau et des corps q'uelle tient en dissolution à l'aide de l'électricité galvanique. *Ann. Chim.* **LVIII**, 54–74 (1806).
25. Duan, C. H. & Majumdar, A. Anomalous ion transport in 2-nm hydrophilic nanochannels. *Nat. Nanotechnol.* **5**, 848–852 (2010).
26. Tunuguntla, R. H., Allen, F. I., Kim, K., Belliveau, A. & Noy, A. Ultrafast proton transport in sub-1-nm diameter carbon nanotube porins. *Nat. Nanotechnol.* **11**, 639–644 (2016).
27. Esfandiar, A. et al. Size effect in ion transport through angstrom-scale slits. *Science* **358**, 511–513 (2017).
28. Chmiola, J. et al. Anomalous increase in carbon capacitance at pore sizes less than 1 nanometer. *Science* **313**, 1760–1763 (2006).
29. Chen, W. et al. Quantum dots of 1T phase transitional metal dichalcogenides generated via electrochemical Li intercalation. *ACS Nano* **12**, 308–316 (2018).
30. Chhowalla, M. et al. The chemistry of two-dimensional layered transition metal dichalcogenide nanosheets. *Nat. Chem.* **5**, 263–275 (2013).
31. Lukatskaya, M. R. et al. Cation intercalation and high volumetric capacitance of two-dimensional titanium carbide. *Science* **341**, 1502–1505 (2013).
32. Lindström, H. et al. $Li^+$ ion insertion in $TiO_2$ (anatase). 2. Voltammetry on nanoporous films. *J. Phys. Chem. B* **101**, 7717–7722 (1997).
33. Augustyn, V. et al. High-rate electrochemical energy storage through $Li^+$ intercalation pseudocapacitance. *Nat. Mater.* **12**, 518–522 (2013).
34. Bankura, A. & Chandra, A. Hydroxide ion can move faster than an excess proton through one-dimensional water chains in hydrophobic narrow pores. *J. Phys. Chem. B* **116**, 9744–9757 (2012).
35. Zhan, C. et al. Specific ion effects at graphitic interfaces. *Nat. Commun.* **10**, 4858 (2019).
36. Dellago, C., Naor, M. M. & Hummer, G. Proton transport through water-filled carbon nanotubes. *Phys. Rev. Lett.* **90**, 105902 (2003).
37. Cheng, C. et al. Ion transport in complex layered graphene-based membranes with tuneable interlayer spacing. *Sci. Adv.* **2**, e1501272 (2016).
38. Cheng, C., Jiang, G. P., Simon, G. P., Liu, J. Z. & Li, D. Low-voltage electrostatic modulation of ion diffusion through layered graphene-based nanoporous membranes. *Nat. Nanotechnol.* **13**, 685–690 (2018).
39. Tao, Q. et al. Two-dimensional $Mo_{1.33}C$ MXene with divacancy ordering prepared from parent 3D laminate with in-plane chemical ordering. *Nat. Commun.* **8**, 14949 (2017).
40. Sheng, L. et al. Multilayer-folded graphene ribbon film with ultrahigh areal capacitance and high rate performance for compressible supercapacitors. *Adv. Funct. Mater.* **28**, 1800597 (2018).
41. Tian, W. Q. et al. Multifunctional nanocomposites with high strength and capacitance using 2D Mxene and 1D nanocellulose. *Adv. Mater.* **31**, 1902977 (2019).
42. Higgins, T. M. et al. Effect of percolation on the capacitance of supercapacitor electrodes prepared from composites of manganese dioxide nanoplatelets and carbon nanotubes. *ACS Nano* **8**, 9567–9579 (2014).

**Publisher's note** Springer Nature remains neutral with regard to jurisdictional claims in published maps and institutional affiliations.

## Methods

**Design and assembly of 2H-$MoS_2$//$LiCoO_2$ soft pack batteries.** 2H-$MoS_2$//$LiCoO_2$ soft pack batteries were fabricated using a commercial processing system. Typically, electrode slurries were first prepared by mixing $LiCoO_2$ (99.8%, Aladdin) or $MoS_2$ (99.5%, Aladdin) powders, super-P and polyvinylidene fluoride dissolved in *N*-methyl pyrrolidone (0.02 g ml$^{-1}$) with a weight ratio of 9:0.5:0.5 for 24 h. Afterwards, the cathode ($LiCoO_2$) or anode ($MoS_2$) slurries were coated to form films on both sides of continuous Al or Cu foils via a roll-to-roll process, respectively. The mass loadings of active materials ($LiCoO_2$ or $MoS_2$) were controlled by the gap distance between the blade and foils during the roll-to-roll process. The obtained electrodes were dried at 90 °C in vacuum for 12 h. The mass loadings (calculated as the total active material's weight on both sides per unit area) for $LiCoO_2$ and $MoS_2$ were 44.2 and 7.4 mg cm$^{-2}$, respectively.

Then, the dried electrode films were punched into sheets with fixed sizes. The obtained $LiCoO_2$ cathode and 2H-$MoS_2$ anode sheets were alternately overlapped with Celgard membranes as separators to assemble soft pack batteries. For one battery, 15 and 14 pieces of cathode and anode sheets were used, respectively. The tabs of the overlapped electrodes were welded with outer metal tabs (Al for cathodes and Ni for anodes). After injecting the electrolyte (1 M $LiPF_6$ in a mixture of ethylene carbonate, diethyl carbonate and dimethyl carbonate, with a volume ratio of 1:1:1) and heat-sealing the Al covers, we obtained the 2H-$MoS_2$//$LiCoO_2$ soft pack batteries. More details of the design and process are described in Supplementary Fig. 3. The mass content of 2H-$MoS_2$ in one soft pack battery was ~4.4 g.

**Preparation of the water suspension of 2D 1T-$MoS_2$ QSs.** Typically, one 2H-$MoS_2$//$LiCoO_2$ soft pack battery was charged at a current density of 0.001 A g$^{-1}$ with a cut-off voltage of 3.2 V. Then, the charged battery was disassembled to collect well-lithiated $MoS_2$ anode sheets. The sheets were first washed with acetone several times to remove the residual surface electrolyte. Then, the sheets were immediately immersed in water under ultrasonication for exfoliation (300 W, 1 h). After the exfoliation process, the obtained exfoliated solution was centrifugally purified (13,000 r.p.m., 30 min) four times to obtain a water suspension of 2D 1T-$MoS_2$ QSs. We obtained ~1.2 g of 1T-$MoS_2$ QSs (~93 wt% in 1T phase purity) from one soft pack battery. The yield was ~27 wt%.

**Preparation of 2D 1T-$MoS_2$ QS films.** 2D 1T-$MoS_2$ QS films were fabricated via a self-developed vacuum filtration method assisted by GO. The detailed process is illustrated in Supplementary Fig. 9.

First, a thin GO nanosheet film was formed on a cellulose acetate filter membrane (47 mm in diameter with average pore size of 250 nm, Millipore). The GO nanosheets were prepared by using a modified Hummers' method[43] on natural graphite flakes (100 mesh, 99.95%, Aladdin). Then, 3 ml of GO water suspension (0.033 mg ml$^{-1}$) was dripped onto the filter membrane to form the GO film via vacuum filtration.

Then, the 2D 1T-$MoS_2$ QS suspension was slowly dripped onto the upper surface of the thin GO film under vacuum filtration. After filtration, a black hydrated 2D 1T-$MoS_2$ QS layer formed on the GO film. The obtained QS/GO/filter sandwich film was immediately immersed in water for autoseparation (Supplementary Fig. 11a). The GO film collapsed and dissolved, leaving an intact QS film in water. The QS film can be easily transferred onto a substrate for further use. The as-obtained QS film bore $H_2O$ molecules confined inside the interlayer space between individual QSs. A dehydrated QS film can be obtained by drying the hydrated film.

2D 1T-$MoS_2$ QS films with different thicknesses (or areal mass loadings) were obtained by controlling the quantity of the filtrated 1T-$MoS_2$ QSs during the vacuum filtration process.

**Preparation of 2D 1T-$MoS_2$ QS electrodes for supercapacitors.** A 100-nm-thick Au layer was coated on the surface of a 100-µm-thick polyimide substrate via magnetron sputtering to serve as a flexible and conductive current collector. Then, a piece of hydrated 2D 1T-$MoS_2$ QS film stored in water was transferred onto the Au/polyimide substrate. After several minutes, the QS film was tightly attached onto the substrate to achieve the hydrated QS electrode. Dehydrated QS electrodes were obtained by naturally drying the as-prepared hydrated QS electrodes for 48 h.

A series of 1T-$MoS_2$ QS electrodes with different thicknesses was prepared. For each thickness, 20 pieces of electrode were prepared under the same conditions. Ten pieces were used for electrochemical tests, and the other ten were used to measure the areal mass loadings and film thicknesses. The areal mass loading of an electrode was determined by the weight and the area of its oven-dried form (treated in a vacuum oven at 90 °C for 4 h). The film thickness was obtained by a statistical cross-sectional analysis on the scanning electron microscopy (SEM) images. The volumetric density was calculated based on the areal mass loading and the film thickness.

**Capillary width measurements.** We have statistically studied the size distribution of our channels for dry films via TEM (Supplementary Fig. 16). The results indicate that all channels are narrower than 1.3 nm. Assuming that the thickness of a $MoS_2$ layer is 0.615 nm, then the capillary channel width is <0.685 nm for dry films. For the hydrated films that deliver high capacitive performance, however, it is difficult to perform TEM measurements due to the high vacuum requirements. Considering that the average channel width expands by 0.55 nm through hydration (XRD results, Fig. 2b) and assuming that the channel size distribution is not substantially altered by hydration, the upper bound of the capillary width for hydrated films would be ~1.235 nm (0.685 + 0.55 nm). Thus, we apply sub-1.2 nm channels throughout the text, consistent with the literature definition[44].

**Electrochemical measurements.** Electrochemical measurements were conducted using a standard three-electrode configuration on an electrochemical workstation (VMP3, BioLogic). Four kinds of electrolytes were used (0.5 M $H_2SO_4$, 0.5 M $Na_2SO_4$, 0.5 M $K_2SO_4$ and 1 M KCl aqueous solution). Typically, a QS electrode was used as the working electrode. For the $H_2SO_4$ electrolyte, a graphite rod (99.9995%, Alfa Aesar) and an electrode formed of Hg/$Hg_2SO_4$ in saturated $K_2SO_4$ were used as the counter electrode and reference electrode, respectively. For $Na_2SO_4$, $K_2SO_4$ and KCl electrolytes, a Pt disk (99.99%, Alfa Aesar) and a saturated calomel electrode were used as counter and reference electrodes, respectively. Linear sweep voltammetry was performed at a scan rate of 2 mV s$^{-1}$ to determine the cyclic voltammetry (CV) scan range (Supplementary Figs. 17a and 19a). CV scans were conducted at scan rates ranging from 5 to 10,000 mV s$^{-1}$. Galvanostatic cycling scans were performed at current densities ranging from 1 to 48 A g$^{-1}$ with the same potential limits of CV scans. The EIS was performed at various potentials versus reference electrodes with frequencies ranging from 1,000 kHz to 0.01 Hz and a sinusoidal voltage of 10 mV.

**Capacitance calculations.** The gravimetric capacitance of an electrode was calculated from CV data using the following formula:

$$C_g = \frac{\int I dV}{Vsm} \tag{1}$$

where $C_g$ is the gravimetric capacitance (F g$^{-1}$), $I$ is the current (A), $V$ is the scan potential range (V), $s$ is the scan rate (V s$^{-1}$) and $m$ is the weight of the electrode (g). The volumetric capacitance ($C_v$, F cm$^{-3}$) or the areal capacitance ($C_a$, F cm$^{-2}$) were calculated by multiplying $C_g$ by the volumetric density (g cm$^{-3}$) or by the areal mass loading (g cm$^{-2}$) of the electrode, respectively.

It should be noted that all the capacitive values in this work were determined based on the parameters of dehydrated electrodes. This method is generally applied for evaluating the electrochemical performance of hydrated 2D-material electrodes[17,21,39,45]. If the effect of nanoconfined water on the weight and size of the electrode was considered, $C_v$ values for the hydrated 1T-$MoS_2$ QS electrodes were approximately two-thirds of the claimed values in this work (see Supplementary Fig. 17b).

**Characterizations.** SEM images were obtained on JSM-7800F Prime field emission SEM equipment (JEOL). The thicknesses of the hydrated films were determined using a Bruker DektakXT surface profiler. X-ray diffraction patterns were collected on a Rigaku D/max 2550 instrument (35 kV, 200 mA) using Cu K$\alpha_1$ radiation (wavelength $\lambda$ = 0.15406 nm). The grazing-incident wide-angle X-ray scattering experiments were performed with a Pilatus3R 300 K detector using Bruker NanoStar small-angle X-ray scattering on the top of a Rigaku H3R rotating anode generator (X-ray Diffraction Shared Experimental Facility at Massachusetts Institute of Technology). We used a small-angle 2 mm beam stop with a sample detector of 109.1 mm for wide-angle X-ray scattering measurements. The exposure time was set as 300 s. Raw wide-angle X-ray scattering patterns were processed with corrections by MATLAB-based GIXSGUI software before analysis. TEM and high-resolution TEM characterizations were conducted on a JEOL JEM-2100F field emission TEM instrument (200 kV). The samples for side-view TEM observations were prepared by embedding the 2D 1T-$MoS_2$ QS films into resin followed by ultrathin sectioning. The atomic-resolution high-angle annular dark-field scanning TEM images were obtained on a JEOL ARM-200F instrument (200 kV) equipped with a cold field emission gun and a Cs corrector for probing lenses. An electron beam shower treatment (~20 min) was conducted before the observation to clean the specimen's surface. UV–vis absorption spectra were recorded on a PerkinElmer Lambda 750 S spectrometer. The atomic force microscope experiments were performed on Bruker Multimode 8 equipment (ScanAsyst mode) under ambient conditions. The samples for atomic force microscope experiments were prepared by dripping the diluted water suspension of 2D 1T-$MoS_2$ QSs onto a mica substrate and then drying under an infrared light for several minutes. XPS data were acquired on a Kratos Axis UltraDLD spectrometer using a monochromatic Al Kα (1486.6 eV) X-ray source. All XPS data were calibrated using the C 1*s* peak (284.8 eV) of adventitious carbon on the sample surface. The Mo 3*d* peaks were fitted using doublets with a 3:2 ($d_{5/2}$:$d_{3/2}$) area ratio, 3.13 eV interval and the same full-width at half-maximum value. Raman spectra were obtained using a Horiba LabRAM HR Evolution Raman microprobe operating with 532 nm excitation. Test conditions were optimized to avoid phase transitions and sample damage during the measurements and to guarantee the stability of the results (objective lens ×50; acquisition time 10 s; accumulated twice). The incidence power on the sample surfaces was ~1.5 mW, below which no Raman signals can be recorded even after a long collection time.

**Computational method.** DFT calculations were performed with the generalized gradient approximation[46], using the plane-wave pseudopotential QUANTUM-ESPRESSO package[47]. Optimized norm-conserving Vanderbilt pseudopotentials were used to describe the interaction between valence electrons and ionic cores[48]. We also included the dispersion correction using the DFT-D3 approach[49]. In all the calculations, the cut-off energy of the plane-wave basis was 40 Ry and the Brillouin zone was sampled using the Γ point. The convergence criteria for structure optimization and single-point calculation were set to $10^{-3}$ Ry bohr$^{-1}$ and $10^{-6}$ Ry, respectively. The 1T-$MoS_2$ monolayer was modelled using an orthogonal supercell consisting of 24 Mo and 48 S atoms, with the optimized lattice parameters of $A = 16.57$ Å and $B = 12.76$ Å. To model the $MoS_2$ surface, the vacuum thickness in the supercell was set to be 20 Å to avoid periodic interactions.

To study ion adsorption on the $MoS_2$ surface in the presence of water, the three-dimensional reference interaction site model (RISM)[50] was used to describe solvation effects. Specifically, in our DFT-RISM calculations, $MoS_2$ and an individual ion were explicitly described by DFT, while the solvent was treated by the RISM approach using the closure model proposed by Kovalenko and Hirata[51], as shown by the coloured medium in Supplementary Fig. 25b. The Lennard-Jones potential and partial charge of the single-point-charge (SPC) water model[52] was used to describe the solvent, while the corresponding parameters of $MoS_2$ and cations were taken from existing studies[53,54].

To simulate $MoS_2$ channels, the channel size *d*, defined by the sulphur–sulphur interlayer distance, was changed using the lattice parameter (*C*, Supplementary Fig. 25a). For a fixed channel size, the optimal water number within the channel was obtained for each ion using a set of single-point energy calculations for varying water number, as reported from our previous work[55]. In addition, the ion–$MoS_2$ interaction energy $E_i$ was computed as the minimum of the energy of ion adsorption referenced to that of the ion in the centre of the channel: $E_i = E_{min} - E_{centre}$. The partial charge transfer from $MoS_2$ to the adsorbed ion was computed via Bader charge analysis[41].

In addition, to better understand the transport properties and hydration structure of solvated ions in the 0.8 nm $MoS_2$ channel, AIMD simulations were carried out using the Vienna Ab initio Simulation Package (VASP)[56] with the identical amount of explicit water predicted by the RISM calculation. In the AIMD simulations, we employed the projector augmented wave potential[57] for nuclei–electron interactions and the Γ point for Brillouin zone sampling. Canonical ensemble simulation was carried out using a Nosé thermostat at 300 K for 24 ps with a time step of 0.5 fs (refs. [58–60]). Structural analysis using the TRAVIS software[61] was conducted using the last 14 ps trajectories after the system was equilibrated for 10 ps.

## Data availability
All the data relevant to the findings of this study have been included in the Supplementary Information.

## Code availability
No customized code was used in this study.

## References

43. Park, S. & Ruoff, R. S. Chemical methods for the production of graphenes. *Nat. Nanotechnol.* **4**, 217–224 (2009).
44. Holt, J. et al. Fast mass transport through sub-2-nanometer carbon nanotubes. *Science* **312**, 1034–1037 (2006).
45. Xu, Y. X. et al. Flexible solid-state supercapacitors based on three-dimensional graphene hydrogel films. *ACS Nano* **7**, 4042–4049 (2013).
46. Perdew, J. P., Burke, K. & Ernzerhof, M. Generalized gradient approximation made simple. *Phys. Rev. Lett.* **77**, 3865–3868 (1996).
47. Giannozzi, P. et al. Quantum ESPRESSO: a modular and open-source software project for quantum simulations of materials. *J. Phys. Condens. Matter* **21**, 395502 (2009).
48. Hamann, D. R. Optimized norm-conserving Vanderbilt pseudopotentials. *Phys. Rev. B* **88**, 085117 (2013).
49. Grimme, S., Antony, J., Ehrlich, S. & Krieg, H. A consistent and accurate ab initio parametrization of density functional dispersion correction (DFT-D) for the 94 elements H–Pu. *J. Chem. Phys.* **132**, 154104 (2010).
50. Nishihara, S. & Otani, M. Hybrid solvation models for bulk, interface, and membrane: reference interaction site methods coupled with density functional theory. *Phys. Rev. B* **96**, 115429 (2017).
51. Kovalenko, A. & Hirata, F. Self-consistent description of a metal–water interface by the Kohn–Sham density functional theory and the three-dimensional reference interaction site model. *J. Chem. Phys.* **110**, 10095 (1999).
52. Matsugami, M., Yoshida, N. & Hirata, F. Theoretical characterization of the 'ridge' in the supercritical region in the fluid phase diagram of water. *J. Chem. Phys.* **140**, 104511 (2014).
53. Heiranian, M., Wu, Y. B. & Aluru, N. R. Molybdenum disulfide and water interaction parameters. *J. Chem. Phys.* **147**, 104706 (2017).
54. Jensen, K. P. & Jorgensen, W. L. Halide, ammonium, and alkali metal ion parameters for modeling aqueous solutions. *J. Chem. Theory Comput.* **2**, 1499–1509 (2006).
55. Sugahara, A. et al. Negative dielectric constant of water confined in nanosheets. *Nat. Commun.* **10**, 850 (2019).
56. Kresse, G. & Furthmüller, J. Efficient iterative schemes for ab initio total-energy calculations using a plane-wave basis set. *Phys. Rev. B* **54**, 11169 (1996).
57. Kresse, G. & Joubert, D. From ultrasoft pseudopotentials to the projector augmented-wave method. *Phys. Rev. B* **59**, 1758–1775 (1999).
58. Nosé, S. A unified formulation of the constant temperature molecular dynamics methods. *J. Chem. Phys.* **81**, 511–519 (1984).
59. Shuichi, N. Constant temperature molecular dynamics methods. *Prog. Theor. Phys. Suppl.* **103**, 1–46 (1991).
60. Bylander, D. & Kleinman, L. Energy fluctuations induced by the Nosé thermostat. *Phys. Rev. B* **46**, 13756–13761 (1992).
61. Brehm, M. & Kirchner, B. TRAVIS—a free analyzer and visualizer for Monte Carlo and molecular dynamics trajectories. *J. Chem. Inf. Model.* **51**, 2007–2023 (2011).


## Acknowledgements

The work at SJTU was supported by the National Natural Science Foundation of China (grant numbers 52072241, 52071213 and 51772187); the Shanghai Science and Technology Committee (grant number 18JC1410500); and the Natural Science Funds for Colleges and Universities in Jiangsu Province, China (grant number 20KJB430048). The work at LLNL was performed under the auspices of the US Department of Energy under contract number DE-AC52-07NA27344. C.Z. and Y.M.W. acknowledge the support of UCOP Project number LFR-17-477237. T.A.P. was supported as part of the Center for Enhanced Nanofluidic Transport, an Energy Frontier Research Center funded by the US Department of Energy, Office of Science, Basic Energy Sciences (BES), under award number DESC0019112. B.D. was supported by the Office of Naval Research (grant number N00014-19-1-2113). We thank R. Luo for his help with TEM characterizations and analyses.


## Author contributions
W.C., J.G., Q.L., D.Z., B.D. and Y.M.W. conceived the idea and designed the experiments. W.C. and M.Y. carried out most of the materials synthesis and electrochemical experiments under the guidance of J.G., Q.L. and D.Z. C.Z. and T.A.P. performed all theoretical calculations. X.Z., G.L. and W.Z. carried out some characterizations and analysis of experiments. W.C., J.G., Q.L. and Y.M.W. wrote the manuscript with contributions from all the co-authors.

## Competing interests
The authors declare no competing interests.

## Additional information
**Supplementary information** The online version contains supplementary material available at https://doi.org/10.1038/s41565-021-01020-0.

**Correspondence and requests for materials** should be addressed to Jiajun Gu, Qinglei Liu, Di Zhang or Y. Morris Wang.

**Peer review information** *Nature Nanotechnology* thanks Xuebin Zhu and other, anonymous, reviewer(s) for their contribution to the peer review of this work.

**Reprints and permissions information** is available at www.nature.com/reprints.